Journal of Magnetic Resonance 309 (2019) 106515

Contents lists available at ScienceDirect

Journal of Magnetic Resonance

journal homepage: www.elsevier.com/locate/jmr

A time domain signal equation for multi-echo spin-echo sequences with arbitrary excitation and refocusing angle and phase

Andreas Petrovic [a,*], Christoph Stefan Aigner [a], Armin Rund [b], Rudolf Stollberger [a,c]

[a] Institute of Medical Engineering, Graz University of Technology, Stremayrgasse 16, 8010 Graz, Austria
[b] Institute for Mathematics and Scientific Computing, University of Graz, Heinrichstrasse 36, 8010 Graz, Austria
[c] BioTechMed-Graz, Austria

ARTICLE INFO

Article history:
Received 5 April 2019
Revised 2 July 2019
Accepted 4 July 2019
Available online 21 September 2019

Keywords:
T_2 mapping
CPMG
CP
Multi-echo spin-echo
Signal model
Generating function

ABSTRACT

Accurate T_2 mapping using multi-echo spin-echo is usually impaired by non-ideal refocusing due to B_1+ inhomogeneities and slice profile effects. Incomplete refocusing gives rise to stimulated echo and so called "T_1-mixing" and consequently a non-exponential signal decay. Here we present a time domain formula that incorporates all relaxation and pulse parameters and enables accurate and realistic modelling of the magnetization decay curve. By pulse parameters here we specifically mean the actual refocusing angle and axis, and phase angle of both the excitation and refocusing pulse. The method used for derivation comprises the so called Generating functions approach with subsequent back-transformation to the time domain. The proposed approach was validated by simulations using realistic RF pulse shapes as well as by comparison to phantom measurements. Excellent agreement between simulations and measurements underpin the validity of the presented approach. Conclusively, we here present a complete time domain formula ready to use for accurate T_2 mapping with multi-echo spin-echo sequences.

1. Introduction

T_2 mapping is an important quantitative magnetic resonance imaging (qMRI) technique investigated by various authors for musculoskeletal [1], liver [2], myocardial imaging [3], as well as neuroimaging [4,5]. However, accurate measurement of T_2 in a clinically feasible time is severely impeded by system imperfections [6–8]. The gold standard for T_2 mapping is the spin-echo sequence where multiple images are acquired with different echo times (TE) and a mono-exponential is fit to the data to calculate T_2 [9]. Certainly, this sequence is too slow to be used in clinical practice. Several faster techniques have been developed including multi-echo spin-echo (MESE) sequences, T_2 prepared gradient echo [10] and EPI [11] and balanced steady-state free precession (SSFP) sequences [12]. In contrast to conventional spin-echo (SE) imaging the MESE sequence uses multiple 180° refocusing pulses after a single 90° excitation resulting in accelerated acquisition. It was originally proposed by Carr and Purcell (CP) [13] and further made more robust against artifacts by Meiboom and Gill (CPMG) [14]. Artifacts in these sequences usually arise due to an inhomogeneous transmit field B_{1+} and non-rectangular slice profiles which both alter the actual flip angle (FA). Refocusing FAs that are not exactly 180° do not only partially refocus the magnetization but also create longitudinal and transversal magnetization. Especially the magnetization that is oriented in the longitudinal direction until the next echo gives rises to stimulated echoes and so-called T_1-mixing [6,7,15–17]. The Meiboom-Gill extension can correct these artifacts for small FA deviations by introducing a 90° phase between excitation and refocusing pulse. However, this correction method breaks down for larger deviations at the border of slice profiles in slice selective pulse sequences. These effects alter the desired mono-exponential signal decay, which is best observed in the first echo being smaller than the second as illustrated in Fig. 1 (therefore the first echo is often excluded from the fitting process). T_2 values fitted to this data using a mono-exponential model are usually overestimated (up to 20%, especially if T_1 is long) [8]. A second source of error is the phase of the excitation and refocusing pulse across the slice, e.g. excitation pulses about the x-axis do not only produce a magnetization component along the y-axis M_y but also some M_x magnetization for which the Meiboom-Gill phase relationship is not true any more, thus experiencing a CP instead of a CPMG sequence.

Several techniques have been proposed to correct for these errors in T_2 mapping, including modifications of the sequence [7,18–23], and applying elaborate models in the fitting process. [24] proposed a dictionary based approach utilizing the full Bloch-equations, [25] used the extended phase graph (EPG)

* Corresponding author.
E-mail address: andreas.petrovic@tugraz.at (A. Petrovic).

https://doi.org/10.1016/j.jmr.2019.07.002
1090-7807/

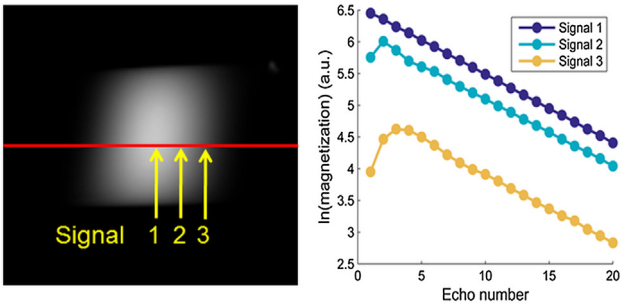

Fig. 1. Measured slice profile and decay curves: The left images shows the magnitude of the magnetization across the slice profile (horizontal direction). On the right the natural logarithms of three decay curves at different positions (indicated in the image on the right) are plotted. The first curve decays mono-exponentially. In contrast, the second curve exhibits a first echo smaller than the second. The third curve is taken from the very edge of the slice profile and is far from being mono-exponential. In classical T_2 quantification the average of all these curves across the profile is measured and mono-exponential models are fitted to it whereas most of the time the first echo is excluded. Data was acquired from a Gadolinium doped water phantom ($T_1 = 137$ ms, $T_2 = 111$ ms) using a CPMG sequence ($\tau = 12$ ms, TR = 1000 ms, 32 echoes, matrix 192×192, voxel size $0.52 \times 0.52 \times 20$ mm^3, phase encoding in slice direction).

algorithm, and [8] applied the Generating Functions (GF) algorithm (z-transform) which utilizes a closed form solution in the z-domain, all with comparable results. All of the methods have their limitations, e.g. the computational effort of solving the Bloch equations, the iterative character of the EPG, or truncation artifacts of the discrete Fourier transform which is necessary to convert the signal decay from the z to the time domain in the GF algorithm.

In this work we present a pure time domain solution for the evolution of the transverse magnetization for MESE sequences with arbitrary excitation and refocusing angle and phase. This solution is based on according to [26] and uses the z-transform to calculate the echo amplitudes. In addition, we incorporated the excitation and refocusing slice profile and analytically inverted the GF to yield a time domain equation. This novel equation was implemented and validated through simulations studies (using the derived formula for simple test cases) and by comparing the simulated signal evolution to MR MESE phantom experiments.

2. Theory

The derivation of the time domain formula consists of three main parts: (1) solution of the Bloch equations for the elementary sequence building blocks (Fig. 2, shaded area) with arbitrary refocusing and excitation pulse parameters, (2) derivation of the z-transform/GF of the signal evolution, and (3) the inversion of the z-transform in order to arrive at an analytical solution in the time domain. Here we will only give the main results, the detailed derivation can be found in the Appendix A.

2.1. Solution of Bloch equation

In a MESE sequence the elementary sequence block that is repeating throughout the sequence after the initial excitation consists of a free precession period $\tau/2$ including relaxation and a dephasing (readout) gradient followed by the refocusing pulse (hard pulse approximation) and another free precession period including the rephasing (readout) gradient (see Fig. 2). The spin dynamics during these periods is governed by the Bloch equation in the case of uncoupled spins with spin quantum number 1/2. It can be solved piecewise for these relaxation, precession and rotation periods. The evolution of the complex magnetization vector $\vec{M} = [M_+, M_+^*, M_z]^T$ (where $M_+ = M_x + iM_y$) during such a block is then given by the difference equation [26]

$$\vec{M}[n+1] = \mathbf{QPQ}\vec{M}[n] + (\mathbf{QP} + \mathbf{I})\vec{S}_{eq} \tag{1}$$

$$\vec{M}[0] = [M_+[0], M_+^*[0], M_z[0]]^T \tag{2}$$

where $\mathbf{Q}$ is a complex matrix accounting for relaxation (κ_1 and κ_2) and free precession $U = e^{i\psi}$ about the z-axis where ψ denotes the phase acquired during precession due to the readout gradient.

$$\mathbf{Q} = \begin{pmatrix} U\sqrt{\kappa_2} & 0 & 0 \\ 0 & U^{-1}\sqrt{\kappa_2} & 0 \\ 0 & 0 & \sqrt{\kappa_1} \end{pmatrix}, \quad \begin{aligned} \kappa_1 &= e^{-\tau/T_1}, \\ \kappa_2 &= e^{-\tau/T_2}, \\ U &= e^{i\psi}, \end{aligned} \tag{3}$$

$\mathbf{I}$ is the unit matrix, the vector S_{eq} accounts for longitudinal relaxation and is given by $\vec{S}_{eq} = [0, 0, M_0(1 - \sqrt{\kappa_1})]^T$, and τ is the inter-echo period. $\mathbf{P} = \mathbf{P}_{\vec{u}}(\alpha)$ is a complex rotation matrix around an arbitrary rotation axis $\vec{u} = [\cos\phi\sin\theta, \sin\phi\sin\theta, \cos\theta]^T$ (ϕ azimuthal angle, θ polar angle, see Fig. 3) about an effective flip angle α and is given by

$$\mathbf{P}_{\vec{u}}(\alpha) = \begin{pmatrix} \lambda & \chi & \nu e^{i\phi} \\ \chi^* & \lambda^* & \nu^* e^{-i\phi} \\ \frac{\nu}{2} e^{-i\phi} & \frac{\nu^*}{2} e^{i\phi} & \zeta \end{pmatrix} \tag{4}$$

with

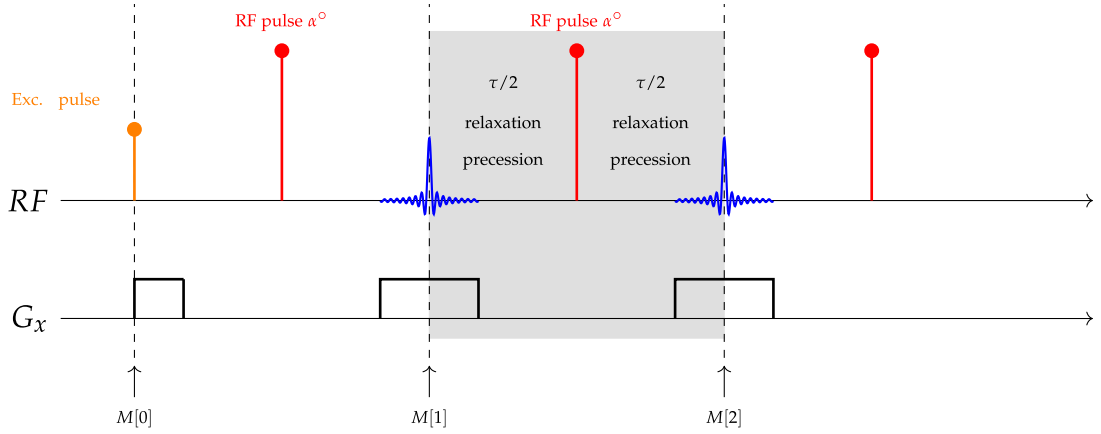

Fig. 2. Sequence diagramm for a MESE sequence: The shaded area corresponds to the repeating sequence building blocks that stay the same from one echo to another. Phase encoding and slice selection gradients are omitted as they are balanced throughout the sequence.

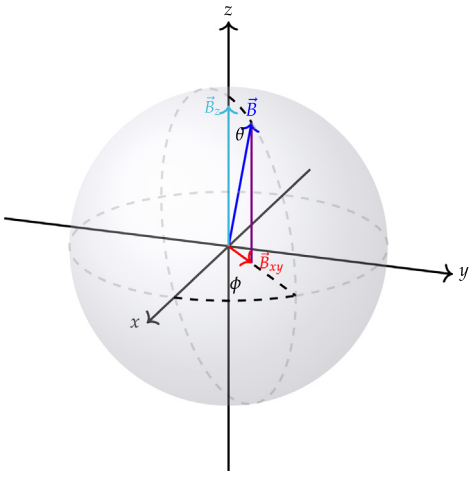

Fig. 3. Definition of coordinate system and angles for the $\vec{B}$ field used in the derivation. The same angles are used for the initial magnetization $\vec{M}[0]$ (θ_e and ϕ_e).

$$\lambda = \left(cos\tfrac{\alpha}{2} - i\sin\tfrac{\alpha}{2}\cos\theta\right)^2, \qquad \chi = e^{2i\phi}sin^2\tfrac{\alpha}{2}sin^2\theta,$$
$$\nu = 2\sin\tfrac{\alpha}{2}\sin\theta\left(sin\tfrac{\alpha}{2}\cos\theta + i\cos\tfrac{\alpha}{2}\right), \quad \zeta = \cos\alpha sin^2\theta + cos^2\theta. \tag{5}$$

In general for repetitive MR sequences the recurrence relation can be written as

$$\vec{M}[n+1] = \mathbf{A}\vec{M}[n] + \vec{B} \tag{6}$$

whereas in this special case $\mathbf{A} = \mathbf{QPQ}$ and $\vec{B} = (\mathbf{QP} + \mathbf{I})\vec{S}_{eq}$ [26].

2.2. z-transform of the difference equation

Introducing the z-transform $\vec{f}(z) = \mathcal{Z}(\vec{M}[n]) = \sum_{n=0}^{\infty}\vec{M}[n]z^n$ and using the shifting property [27] one obtains an expression for the z-transformed difference equation $\vec{M}[n+1] = \mathbf{A}\vec{M}[n] + \vec{B}$ as follows: The z-transform of $\vec{M}[n+1]$ can be easily obtained as

$$\mathcal{Z}(\vec{M}[n+1]) = \sum_{n=0}^{\infty}\vec{M}[n+1]z^n = \vec{M}[1] + \vec{M}[2]z + \cdots + \vec{M}[\infty]z^{\infty} \tag{7}$$

$$= z^{-1}\left(\sum_{n=0}^{\infty}\vec{M}[n]z^n - \vec{M}[0]\right) = z^{-1}\left(\mathcal{Z}(\vec{M}[n]) - \vec{M}[0]\right) \tag{8}$$

As the sequence is causal and all values for negative n are zero the additive factor $\vec{B}$ can be thought of as a function $\vec{B}[n] = \vec{B}u[n]$ where $u[n]$ is the unit step function. Transforming this expression yields the sum of the geometric series (requiring $|z| < 1$ for convergence)

$$\sum_{n=0}^{\infty}\vec{B}u[n]z^n = \frac{1}{1-z}\vec{B} = \frac{z^{-1}}{z^{-1}-1}\vec{B} \tag{9}$$

Putting all this together one arrives at the z-transformed difference equation:

$$z^{-1}(\mathcal{Z}(\vec{M}[n]) - \vec{M}[0]) = \mathbf{A}\mathcal{Z}(\vec{M}[n]) + \frac{z^{-1}}{z^{-1}-1}\vec{B}. \tag{10}$$

$\vec{M}[0]$ is the initial magnetization (i.e. after excitation) $\vec{M}[0] = M_0[\cos\phi_e\sin\theta_e, \sin\phi_e\sin\theta_e, \cos\theta_e]^T$ and M_0 the equilibrium magnetization. Solving for $\vec{f}(z)$ gives a closed form solution for the z-transform of the magnetization evolution

$$\vec{f}(z) = (\mathbf{I} - z\mathbf{A})^{-1}\left(\vec{M}[0] + \frac{z}{1-z}\vec{B}\right). \tag{11}$$

$\vec{f}(z)$ accounts for the magnetization evolution for every single isochromate. To obtain an expression that accurately models the evolution of the signal in a MESE sequence averaging over the individual isochromates is necessary. This can be achieved utilizing the residue theorem of complex analysis [26] yielding an averaged function $\vec{f}_0(z) = [F_0, F_0^*, L_0]^T$ with the relevant component F_0 accounting for the transverse magnetization (L_0 models the evolution of the longitudinal magnetization). A detailed description of the averaging process can be found in Appendix A. After this step and subsequent rearrangement of terms the resultant expression is given as:

$$F_0(z) = \frac{M_0 e^{i\phi}\sin\theta_e}{2}\left[cos(\phi_e - \phi)\left(1 + \sqrt{\frac{X_+(z)}{X_-(z)}}\right) + i\sin(\phi_e - \phi)\left(1 + \sqrt{\frac{X_-(z)}{X_+(z)}}\right)\right], \tag{12}$$

$$X_+(z) = (1 + z\kappa_2)(1 - z(\cos\alpha sin^2\theta + cos^2\theta)(\kappa_1^+ + \kappa_2) + z^2\kappa_1\kappa_2) \tag{13}$$

$$X_-(z) = (1 - z\kappa_2)(1 - z(\cos\alpha sin^2\theta + cos^2\theta)(\kappa_1^- - \kappa_2) - z^2\kappa_1\kappa_2) \tag{14}$$

The first term in the square brackets describes the signal for a CPMG sequence and the second one for a CP sequence, respectively (see also Ref. [26]). The factor $cos(\phi_e - \phi)$ is the amount of initial magnetization that is projected onto the orientation of the refocusing B_1+ field in the xy-plane, and $sin(\phi_e - \phi)$ the amount that is projected onto the perpendicular orientation. This is not surprising since the magnetization that is aligned with the refocusing rotation axis experiences a CPMG sequence and perpendicular magnetization experiences a CP sequence. The polar angle of the refocusing axis θ enters the equation through the effective flip angle which is defined by $cos\alpha_e = \cos\alpha sin^2\theta + cos^2\theta$ [26]. After computation of the signal evolution, the previous projection has to be undone by rotating the resulting transverse magnetization back to its original orientation by multiplying by $e^{i\phi}$. $M_0\sin\theta_e$ is exactly the amount of magnetization converted to transversal magnetization by the excitation pulse (for previously fully relaxed equilibrium magnetization). The reader should not confuse the specific angles for excitation and refocusing pulse, namely the excitation pulse profile expressed in polar coordinates θ_e and ϕ_e, and the rotation axis θ and the phase ϕ of the refocusing pulse, respectively. The former describe the excited magnetization in spheric coordinates, whereas the latter define the rotation axis of the refocusing pulse. The expression incorporating the excited magnetization in Cartesian coordinates can be found in the Appendix A.

Principally, Eq. (12) can already be used to calculate the echo amplitudes for a MESE sequence. Bearing in mind that the z-transform reduces to the discrete time Fourier transform (if it exists) for $z = e^{i\varphi}$, and moreover to the discrete Fourier transform (DFT) for equidistantly sampled values of φ, i.e. $\varphi_k = \frac{2\pi k}{K}$ and $k = 0, \ldots, K-1$, the echo amplitudes are obtained using the inverse DFT of $F_0(e^{i\varphi_k})$ evaluated around the unit circle. However, the DFT can cause problems through truncation/leakage effects which results in flawed echo amplitudes [8]. Therefore, a method to analytically transform $F_0(z)$ to the time domain is desireable.

2.3. Derivation of time domain formula

For inverse z-transform of (12) first the arguments of the square roots are treated. Here we obtain rational functions $Y_\perp(z) = X_+(z)/X_-(z)$ and $Y_{||}(z) = X_-(z)/X_+(z)$, that can be inversely

transformed using e.g. Mathematica. Doing that one arrives at a time domain expression $\eta[n]$, which is a convolution of the inverse z-transform of the root itself according to the convolution property ($(x[n] * x[n] \circ\!\!-\!\!\bullet\, X(z)^2)$.). Thus,

$$Y_{\perp}(z) \bullet\!\!-\!\!\circ^{z^{-1}} \eta_{\perp}[n] = g_{\perp}[n] * g_{\perp}[n] \quad \text{and} \quad Y_{\parallel}(z) \bullet\!\!-\!\!\circ^{z^{-1}} \eta_{\parallel}[n] = g_{\parallel}[n] * g_{\parallel}[n]. \tag{15}$$

The actual time domain contribution of both magnetization components $g_{\perp}[n]$ and $g_{\parallel}[n]$ experiencing a CPMG and a CP sequence, respectively, can subsequently be obtained by deconvolution of the corresponding functions $\eta_{\perp}[n]$ and $\eta_{\parallel}[n]$. Since the system is causal ($\eta_{\perp,\parallel} = 0$ for all $n < 0$) the deconvolution is given recursively as

$$g_{\perp,\parallel}[n] = \begin{cases} \sqrt{\eta_{\perp,\parallel}[0]} & n = 0 \\ \dfrac{\eta_{\perp,\parallel}[n] - \sum_{k=1}^{n-1} g_{\perp,\parallel}[k] g_{\perp,\parallel}[n-k]}{2\sqrt{\eta_{\perp,\parallel}[0]}} & n \geqslant 1 \end{cases} \tag{16}$$

with $\eta_{\perp,\parallel}[0] = 1$. A detailed derivation of these functions is given in the Appendix A. Finally, the constant terms 1 in (12) inversely transform to a Dirac delta function $\delta[n]$. In summary, the combined and actually measured signal, i.e. the n^{th} echo at echo time $n \cdot \tau$, can be computed as

$$M_{+}[n] = \frac{M_0 e^{i\phi} \sin\theta_e}{2} \Big[cos(\phi_e - \phi)(g_{\perp}[n] + \delta[n]) + i \sin(\phi_e - \phi)(g_{\parallel}[n] + \delta[n]) \Big] \quad n \geqslant 0. \tag{17}$$

For $n = 0$ this reduces to the magnetization directly after the excitation pulse $M_{+}[0] = M_0 e^{i\phi_e} \sin\theta_e$.

3. Methods

3.1. Simulations

3.1.1. Signal evolution for CPMG, CP, and mixed type MESE sequences

Six signal evolutions for various parameter combinations where simulated and plotted. Parameters where chosen as (a) excitation around x-axis, refocusing around y-axis (CPMG sequence), (b) excitation around y-axis, refocusing around x-axis (CPMG sequence), (c) excitation and refocusing around y-axis (CP sequence), (d) excitation around an axis of 45°, refocusing around −45° (CPMG sequence with additional phase), (e) excitation around an axis of 135°, refocusing around x-axis (mixed CP and CPMG sequence), (f) excitation around y-axis and refocusing around an axis of 45° (mixed CP and CPMG sequence). The other parameters were fixed for all simulations $M_0 = 1$ a.u., $T_1 = 1000$ ms, $T_2 = 100$ ms, echos spacing $\tau = 10$ ms, excitation angle $\theta_e = 90^{\circ}$, refocusing angle $\alpha = 180^{\circ}$ and polar angle of the refocusing axis $\theta = 90^{\circ}$.

3.1.2. Simulation of the evolution of the slice profile

In this experiment the evolution of a whole slice profile was computed. The numerical waveforms of RF amplitude and phase and the slice selection gradient where fed into the forward Shinnar-Le Roux (SLR) algorithm [28] to compute the corresponding final Cayley-Klein parameters a and b for the accumulated effect of the RF pulse.

For the excitation pulse the excitation magnetization profile was computed using $M_{+} = 2ab^{*}$ (assuming initially fully relaxed magnetization $\vec{M} = [0, 0, M_0]^T$). This profile was then converted to spherical coordinates and parameters $\theta_e(z)$ and $\phi_e(z)$ were extracted (z denoting the spatial coordinate in slice direction).

For the refocusing pulse the computation of the actual refocusing profile is not necessary. Instead the relations between the parameters a and b and the parameters α, θ, and ϕ given in the publication by Pauly [28] were inverted.

$$\alpha = 2arccos\Re(a) \tag{18}$$

$$\phi = arctan - \frac{\Re(b)}{\Im(b)} \tag{19}$$

$$\theta = arctan \frac{-be^{-i\phi}/i}{-\Im(a)} \tag{20}$$

This yields the spatially dependent parameters $\alpha(z)$, $\phi(z)$, and $\theta(z)$ that can be directly inserted in the previously derived formula (z again denoting the spatial coordinate). Care must be taken implementing the *arctan* functions, e.g. for the simulations in this publication the Matlab (Mathworks Inc., Natick, MA) function atan2 was used. The remaining parameters used in the simulations were $M_0 = 1$ a.u., $T_1 = 137$ ms, $T_2 = 111$ ms, and $\tau = 12$ ms. The results were plotted in a 3D plot to illustrate the alterations of the signal decay when moving through the slice profile.

3.2. Comparison with measurements

To compare the signals computed with the derived formula the simulated and measured evolution of the slice profile were compared. Therefore data for a CPMG (exc. y-axis, refoc. x-axis) and a CP sequence (both exc. and refoc. y-axis) were measured in a Gadolinium doped water phantom ($T_2 = 111$ ms and $T_1 = 137$ ms) on a 3 T scanner (Skyra, Siemens). Pulse sequence parameters were: echo spacing $\tau = 12$ ms, TR = 1000 ms, nominal excitation flip angle $\beta = 90$ and nominal refocusing flip angle $\alpha = 180^{\circ}$. The standard Siemens MESE sequence was modified such that the read out gradients were applied in the slice-direction to obtain the slice signal evolution across the slice profile.

3.3. Fitting

The superior performance of models including B_{1+}-inhomogeneities and slice profiles for T_2-mapping using the GF approach [26] was already demonstrated in [8]. To asses the accuracy and precision of the algorithm applied to least squares fitting of "bi-exponential" relaxation data with two T_2 components T_{2s} (short) and T_{2l} (long) the following experiments were performed.

1. Fitting of simulated data to assess accuracy and precision of the model: T_2 values were chosen to mimic normal white brain matter [29]. Complex MSE data were simulated with parameters $\tau = 10$ ms for $T_{2l} = 100$ ms ($M_{0l} = 40$ a.u.) and $T_{2s} = 15$ ms ($M_{0s} = 10$ a.u.) and $T_1 = 1000$ ms. Both decay curves were added together and Gaussian noise with was added to the real and imaginary part of the data. Noise standard deviation was computed to achieve 3 different SNRs (SNR = 80, 60, 40). For each SNR the fitting was repeated with different noise

$N = 200$ times and median values and the 25% and 75% quantiles of the fitted parameters where evaluated.

2. Fitting of acquired white matter data to asses feasibility in brain T_2-mapping: For 183 white matter pixels T_2 values were estimated using our method, bi-exponential and mono-exponential least-squares fitting. Mean values and standard deviation were compared between the methods. The CPMG sequence parameters were TR = 4000 ms, $\tau = 10$ ms, 25 echoes, matrix 192×192, voxel size $1.3 \times 1.3 \times 4$ mm^3. The B_{1+} map was acquired with a sequence employing the Bloch-Siegert shift [30].

4. Results

4.1. Simulations

4.1.1. Signal evolution for CPMG, CP, and mixed type MESE sequences

In Fig. 4 the results of the simulations for CPMG, CP and mixed type MESE sequences are shown. (a) corresponds to a standard CPMG sequence. As the excitation is carried out around the x-axis, only M_y (i.e. negative imaginary part) is present. This magnetization is refocused around the y-axis and therefore doesn't oscillate but stays negative while decaying. (b) is basically the same scenario as in (a) with the only difference that excitation and refocusing axis are switched. This results in a decaying positive real component M_x without oscillations. Fig. 4(c) corresponds to a classic CP sequence with excitation and refocusing around the y-axis. The resulting decay has only a real component M_x but oscillates between positive and negative values after every refocusing pulse. In (d) the phase between excitation and refocusing pulse is 90° (i.e. CPMG) but both rotation axes are turned −45°. This results in a CPMG like decay (no oscillations) with the overall magnetization split into a positive real and negative imaginary part with initial magnitude of $1/\sqrt{2}$. Fig. 4(e) shows the magnetization decay after an excitation around an axis of 135° (resulting in magnetization aligned $\phi_e = 45^\circ$ between x and y-axis). Refocusing is performed around the x-axis, so that the magnetization amount along the x-axis (real part) experiences a CPMG sequence (no oscillations), and the amount along the y-axis a CP sequence (oscillations). Finally, in (f) also a mixed-type sequence is shown with excitation around the y-axis (resulting in $\phi_e = 0^\circ$) and refocusing around a $\phi = 45^\circ$ axis. The difference compared to (e) is that here the different magnetization amounts experiencing a CP or CPMG sequence are mixed together when they are read out giving rise to oscillations in both the real and imaginary part. These intuitive test cases all support the validity of the presented formula.

4.1.2. Simulation of the evolution of the slice profile

In Fig. 5 the used RF pulses and their corresponding slice profiles or pulse parameters α, θ and ϕ are shown. In (a) and (b) the excitation and refocusing pulses are displayed. Fig. 5(c) illustrates the magnitude as well as x and y components of the transverse magnetization after a 90° excitation using the pulse in (a) computed with the forward SLR algorithm. Excitation was obviously carried out around the y-axis as the main component of the magnetization is aligned with the x axis thereafter. However, some residual magnetization is left along the $+$ and $-y$ axes. The parameters α, ϕ and θ for the refocusing pulse were extracted from the SLR parameters a and b and are displayed in Fig. 5(d)–(f).

In Fig. 6 the simulated evolution of the magnetization for a CPMG (exc. y-axis, refoc. x-axis) are plotted. In (a) and (b) the whole slice profile and selected decay curves ($1 = \text{middle} \ldots 4 = \text{edge}$) are given for M_x and in (c) and (d) for M_y, respectively. In (b) it can be seen that most decay curves exhibit a large magnetization drop already after the first refocusing

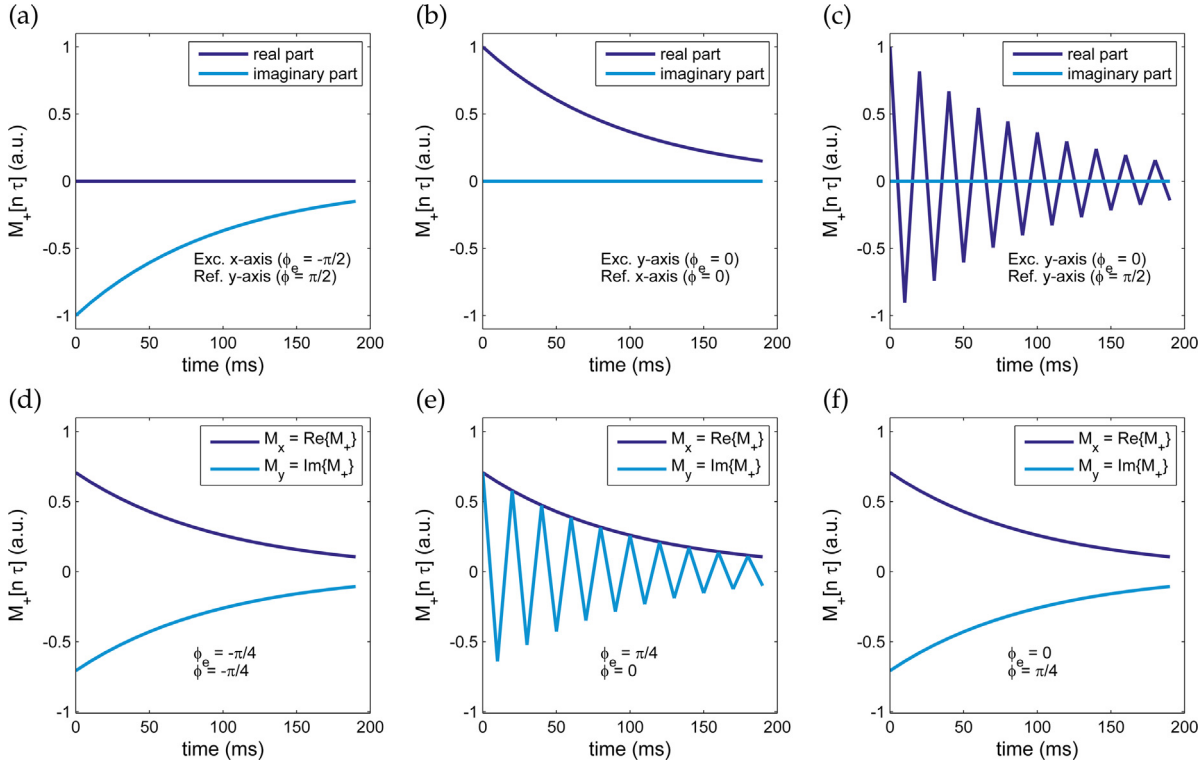

Fig. 4. Simulation of signal evolution for (a) excitation around x-axis, refocusing around y-axis (CPMG sequence), (b) excitation around y-axis, refocusing around x-axis (CPMG sequence), (c) excitation and refocusing around y-axis (CP sequence), (d) excitation around an axis of 45°, refocusing around −45° (CPMG sequence with additional phase), (e) excitation around an axis of 135°, refocusing around x-axis (mixed CP and CPMG sequence), (f) excitation around y-axis and refocusing around an axis of 45° (mixed CP and CPMG sequence).

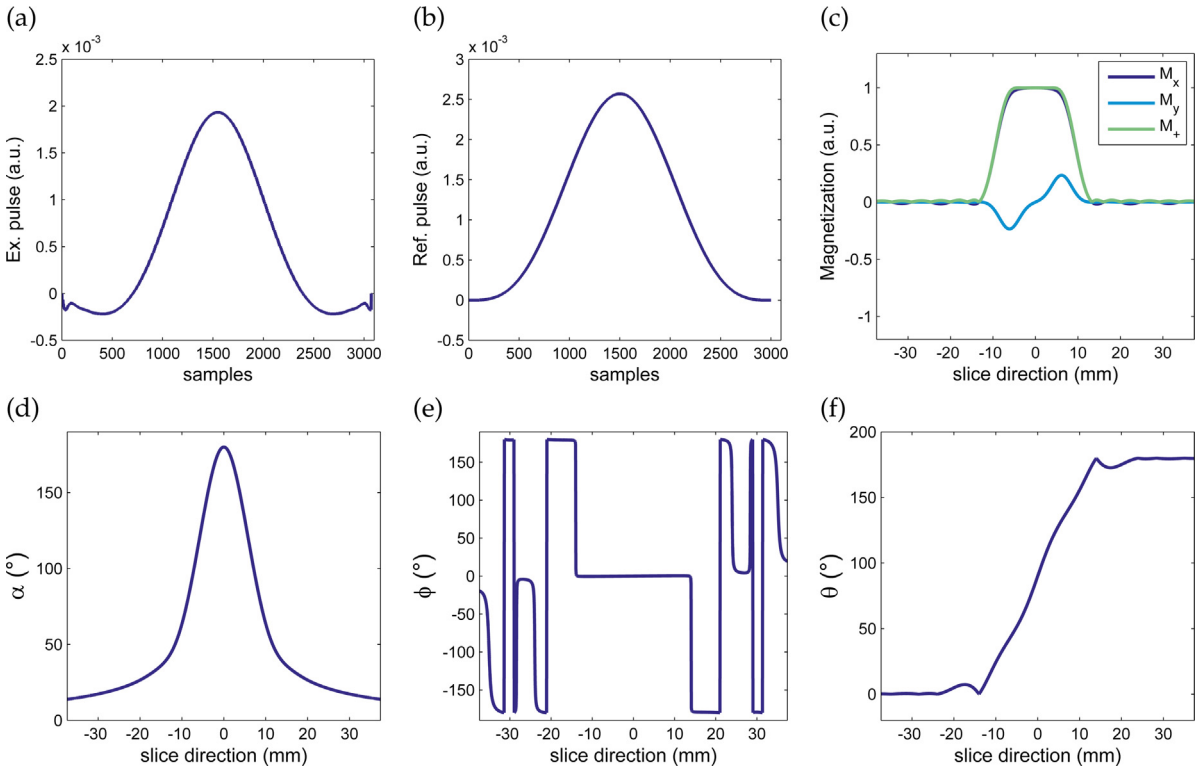

Fig. 5. (a) RF waveform of excitation pulse, (b) RF waveform of refocusing pulse, (c) excitation pulse profile, (d) refocusing angle profile, (e) refocusing azimuthal angle (i.e. refocusing phase) profile, and (f) refocusing polar angle (i.e. refocusing axis) profile, all computed using forward SLR algorithm.

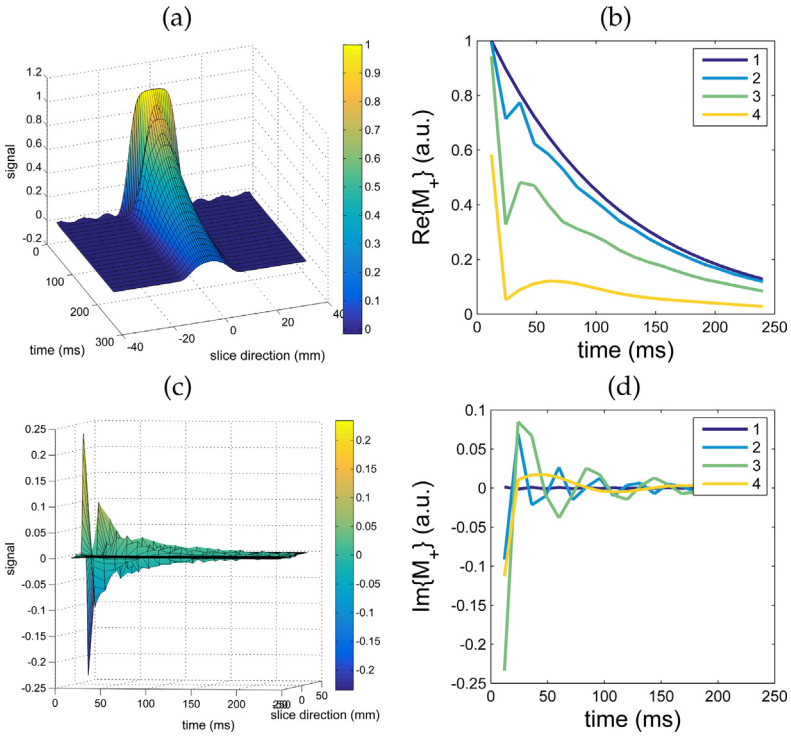

Fig. 6. (a) Evolution of the slice profile for M_x, (b) selected M_x decay curves, (c) evolution of the slice profile for M_y, (b) selected M_y decay curves. For (b) and (d) numbers 1 correspond to the middle of the slice profile going to 4 at the edge of the profile.

pulse when the flip angle is not 180 (curves 2–4). The subsequent decay is also slower, as described previously [8]. In (d) the signal curve 1 is zero at all times because the excitation pulse did not produce magnetization in the middle of the slice profile along the y-axis. The other curves (3–4) alternate between positive and negative values.

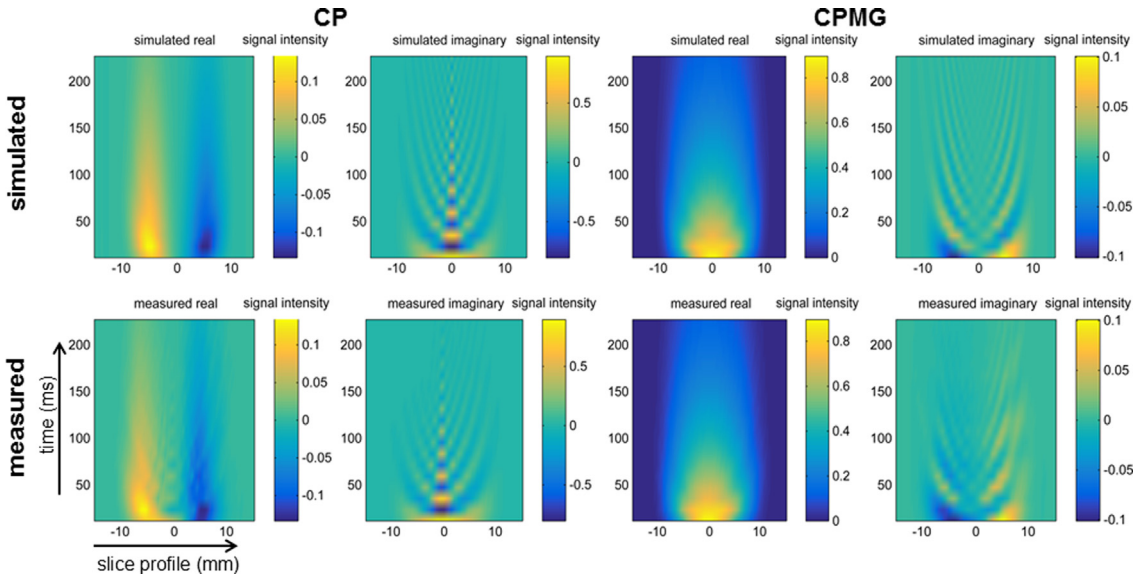

Fig. 7. Comparison between simulation and measurements: The top row are simulations, the bottom row the corresponding measurements. On the left hand side the signals for a CP sequence are compared, on the right hand side signals for a CPMG sequence, respectively. For each sequence type both real and imaginary part show excellent agreement between simulation and measurement.

4.2. Comparison with measurements

In Fig. 7 simulated (top row) and measured (bottom row) signals for a CP (left) and CPMG (right) sequence are plotted. For each plot the horizontal position corresponds to a position across the slice profile and the vertical position to the time evolution of the signal, respectively. First of all, comparing simulation and measurement (top and bottom row) one can observe excellent agreement between those two. For the CP sequence with excitation around the x-axis the major part of the magnetization is flipped to the $-y$-axis (imaginary part) and a smaller portion with negative parts on the left and positive parts on the right of the slice profile is flipped to the $-x/x$-axis (real part). The real part then experiences a CPMG sequence and therefore keeps its sign throughout the echo evolution, whereas the imaginary part has alternating sign. Both have in common that the magnetization is decaying. The imaginary part decays with T_2 in the center where the flip angle is close to 180°, but faster than T_2 at the border of the slice due to imperfect refocusing. The pure T_2 decay cannot be seen in the real part, as there is no initial magnetization at the center of the slice. For the CPMG sequence the main part of the magnetization is aligned along the x-axis after excitation. It is refocused around this axis and therefore keeps its sign and again decays with T_2 in the middle of the slice and faster at the edges. The part of the magnetization that is initially aligned along the $-y/y$-axis experiences a CP sequence and therefore changes sign after a couple of pulses.

4.3. Fitting

The results for the fitting simulation are summarized in Table 1 where median values and upper and lower quantiles are compared to the simulation ground truth values. For the long T_2 species both M_0 and T_2 were fitted with good accuracy and precision. For the short T_2 species deviations were bigger but still acceptable, especially for the T_{2s} value. The estimations generally tend to get worse with decreasing SNR level.

For the fitting to acquired MR data of normal white matter the following results were obtained for the proposed model compared to conventional bi-exponential fitting (subscript *bi*) and mono-exponential fitting (subscript *mo*): Mono-exponential $T_{2,mo} = 96.6 \pm 3.0$ ms, bi-exponential $T_{2s,bi} = 43.1 \pm 6.4$ ms and $T_{2l,bi} = 121.5 \pm 8.5$ ms, and the GF model $T_{2s} = 27.8 \pm 5.4$ ms and $T_{2l} = 87.2 \pm 5.8$ ms (all values are mean $\pm$ standard deviation). This observation that $T_{2,bi}$ are longer than T_2 coincides with the results for mono-exponential fitting [8] where T_2 values are usually overestimated using the standard mono-exponential approach. Mono-exponential fitting yields a result located in between $T_{2s,bi}$ and $T_{2l,bi}$. Standard deviations are in a reasonable range for all methods.

Values for M_0 are not given here as they are influenced by the slice profile incorporation as well as the local sensitivity of the receive coils.

5. Discussion and conclusion

In this work we present a time domain formula for the evolution of the transverse magnetization in multi-echo spin-echo sequences. The derived formula is a continuation and generalization of the Generating functions method first published by Lukzen [31,26]. For a repetitive sequence building block a solution of the Bloch equation is computed and, subsequently, the established

Table 1
Results of the bi-exponential fitting simulations. In comparison to the ground truth median values and 25% and 75% quantiles are given for 3 different SNR values (N = 200). Median values were tested for significance using a sign test (significance level $\alpha = 0.05$).

		SNR = 80			SNR = 60			SNR = 40		
	Ground truth	0.25	0.5	0.75	0.25	0.5	0.75	0.25	0.5	0.75
M_{0s} (a.u.)	**10**	9.7	**10.6** ($p < 0.05$)	11.9	9.4	**10.8** ($p < 0.05$)	12.1	10.3	**12.7** ($p < 0.05$)	16.1
M_{0l} (a.u.)	**40**	39.3	**39.9** ($p = 0.21$)	40.7	38.4	**39.9** ($p = 0.34$)	40.7	38.2	**39.9** ($p = 0.52$)	41.1
T_{2s} (ms)	**15**	11.9	**15.2** ($p = 0.73$)	18.1	12.2	**16.1** ($p = 1.00$)	20.1	9.1	**14.0** ($p = 0.65$)	21.2
T_{2l} (ms)	**100**	98.5	**100.0** ($p = 0.10$)	101.7	98.8	**100.4** ($p = 0.80$)	103.0	97.8	**100.6** ($p < 0.05$)	103.5

recurrence relation is solved using the z-transform. This method works for all sequences consisting of repeating building blocks. Theoretically, the method can be extended also to coupled or exchanging spins using e.g. the Bloch-McConnell equation. For spins $> 1/2$ one could also use the master equation of the density matrix, although the equations might get intractable quite soon.

Simulations for test cases are all in agreement with the expected signal decay. Furthermore, when compared to measurements also excellent congruence between simulation and measurement could be observed. The provided formula contains all relevant excitation and refocusing parameters that are used in the MESE sequence. First, the initial excitation profile is incorporated with the flip angle θ_e and the phase angle ϕ_e, and, second, the refocusing axis and angle by the parameters θ, ϕ, and α. Using θ_e and ϕ_e an arbitrary magnetization preparation preceding the refocusing train can be used. Naturally, also the equilibrium magnetization M_0, relaxation parameters T_1 and T_2, as well as sequence timing τ are included. Compared to the generating functions approach, where the z-transform is evaluated at points around the unit circle $z = e^{i\phi_k}$ and subsequently the inverse DFT is applied, no leakage effects from the transformation are possible, which is especially relevant for long T_2 as in blood [32], peritumoral edema [33] or CSF [34] (see Fig. 8). The derived formula is an exact solution without any approximations.

In the limiting case of 180° refocusing pulse the formula degenerates to a simple and an alternating sign exponential decay, for CPMG and CP type sequences, respectively. It is readily implemented and evaluated by the computation of the sum of 3 exponential functions and a discrete deconvolution step which can also be exactly calculated due to the causal nature of the signals. Compared to other methods, such as Bloch matrices or EPG, no consecutive multiplication of nutation and precession matrices is necessary, and additionally the formula inherently keeps track of all relevant isochromats.

In the case of 2D T_2-mapping the knowledge of the actual angle and phase of the pulses across the slice is crucial. all pulse parameters are discretized along the slice direction giving a vector α_j, and equivalently for θ_j and ϕ_j where subscript j accounts for discretization across the slice profile. This gives the following expression for the measured signal pixelwise integrated across the slice profile:

$$M_+^{SP}[n] = \frac{1}{Q}\sum_{j=1}^{Q} \frac{M_0 e^{i\phi_j}\sin\theta_{e,j}}{2}\left[cos(\phi_{e,j}-\phi_j)(g_\perp[n,j]+\delta[n]) + isin(\phi_{e,j}-\phi_j)(g_{||}[n,j]+\delta[n])\right] \quad n \geqslant 0. \tag{21}$$

where SP denotes integration across the slice and Q is the number of discretization points. Basically, α_j, θ_j and ϕ_j are computed from the refocusing pulse shape (θ_e and ϕ_e for the excitation pulse, respectively) using the SLR algorithm which takes the actual B_{1+} and B_0 values as input values for every pixel. Therefore, B_{1+} mapping, e.g. by [35,30] is necessary beforehand. However, it was also shown in [8] that the B_{1+} map can be fitted itself under certain conditions. In a clinical setting B_0 inhomogeneities usually slightly alter the slice position and thickness (if gradients are present). To our experience this effect is negligible and, therefore, no additional B_0 mapping is required.

T_2-fitting is then for example accomplished by least-squares minimization of the following functional when magnitude image data $d[n]$ are used:

$$[\hat{M}_0, \hat{T}_2] = arg \min_{M_0,T_2} \| d[n] - |M_+^{SP}[n]| \|_2^2 \tag{22}$$

In the case of a long and short T_2 species such as free and myelin-bound water usually bi-exponential fits are computed. Bi-exponential fitting itself is an ill-posed problem [36] and a sufficiently high SNR in combination with a substantial difference between T_{2s} and T_{2l} required to obtain reliably results. Certainly, if exact fitting is possible, multi-parametric models can provide additional specific information for certain tissues. Our accurate model will further improve T_2 mapping for these tissues.

In a simulation experiment we demonstrated the feasibility of the proposed model for multi-parameter estimation and presented values on the accuracy and precision of the method for different SNRs. For the fitting of acquired brain data the incorporation of the slice profile yielded lower values for T_2 as was already demonstrated for the case of a single T_2 species [8]. Mono-exponential fitting yielded results between the bi-exponential T_2 values and although this is certainly the wrong model a reasonably good fit was achieved. The values obtained by our method tend to approach the values Whittall et al. presented in [29]. This is good evidence for the effectiveness of our method as these authors employ a single slice CPMG sequence with rectangular (hard) refocusing pulses to eliminate slice profile effects. Furthermore, they report a generally larger standard deviation for T_{2s} in simulation experiments which is also reflected in our observations.

We believe this approach is a valuable and ready to use method that can be used for more accurate and comparable T_2 quantification and will be of great value for model-based MRI reconstruction techniques in the future as we already demonstrated at an earlier stage [37]. Therefore, we also decided to make a C/C++ version of

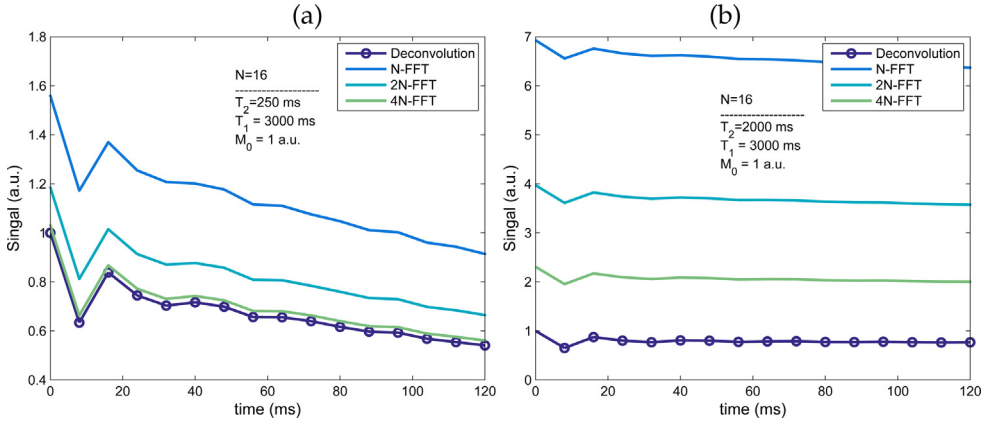

Fig. 8. Illustration of leakage effect using the DFT approach compared to the presented method for (a) blood ($T_2 \approx 250$ ms) and (b) CSF ($T_2 \approx 2000$ ms) for different DFT lengths. Other simulation parameters where $M_0 = 1$ a.u., $T_1 = 3000$ ms, $\tau = 8$ ms, 16 echoes. The shorter the computed DFT the more the deviation from the actual signal decay becomes apparent.

the core algorithm available to the scientific community. The source files will for downloadable under http://www.t2mapping.rocks.

Acknowledgements

Partial support from "SFB F32-N18" and BioTechMed-Graz are gratefully acknowledged.

Appendix A. Derivation

In this section a detailed description of how to set up the framework for the generating functions approach for a classic CP/CPMG sequence is described. A complete derivation of the GF starting from the recursive solution of the Bloch equations is presented. Z-transformation of the recurrence relations will give a GF for every single isochromate. As the CP/CPMG sequence is not balanced, i.e. the net read out gradient area between two pulses is not zero, many different spin configurations will be produced by the repeating RF pulses. In this case, to yield the desired echo amplitudes, the GF for the zeroth configuration (i.e. no phase at the time of the echo) has to be computed by complex contour integration.

The specific sequence considered here is a MESE sequence starting with an arbitrary initial magnetization $\vec{M} = [M_+, M_+^*, M_z]^T$ and refocusing pulses that rotate around an arbitrary axis about an angle α.

A.1. z-transform of recurrence relation

As shown in Section 2.1 the recursive solution of the Bloch equations can be generally given by

$$\vec{M}[n+1] = \mathbf{A}\vec{M}[n] + \vec{B} \tag{A.1}$$

where in this special case $\mathbf{A} = \mathbf{QPQ}$ and $\vec{B} = (\mathbf{QP} + \mathbf{I})\vec{S}_{eq}$. After z-transform it follows in (11)

$$\begin{aligned}\vec{f}(z) &= \mathcal{Z}(\vec{M}[n]) = [F(z), F^*(z), L(z)]^T \\ &= (\mathbf{I} - z\mathbf{A})^{-1}\left(\vec{M}[0] + \frac{z}{1-z}\vec{B}\right)\end{aligned} \tag{A.2}$$

where $\vec{M}[0]$ is an arbitrary initial magnetization resulting after excitation of the spin system $\vec{M}^{(0)} = [M_x + iM_y, M_x - iM_y, M_z]^T$. Evaluating this expression gives a vector of three rational functions of which only the first $F(z)$ is of interest concerning the transverse magnetization. Next, it is useful to group the terms in numerator and denominator in $F(z)$ according to the powers of U, as we now have to average over the isochromates. After collection the terms we end up with the following expression:

$$F(z) = \frac{c_0 + c_1U + c_2U^2 + c_3U^3}{d_0 + d_1U^2 + d_2U^4} \tag{A.3}$$

with coefficients

$$\begin{aligned}
c_0 &= -M_+z\kappa_2(1-z)(1-z\kappa_1)\left(\cos\theta\sin\tfrac{\alpha}{2} - i\cos\tfrac{\alpha}{2}\right)^2,\\
c_1 &= -2e^{i\phi}z^2\kappa_2^{3/2}(M_z\sqrt{\kappa_1}(1-z) + M_0(1-\sqrt{\kappa_1})(1+z\sqrt{\kappa_1}))\sin\tfrac{\alpha}{2}\sin\theta\left(\cos\theta\sin\tfrac{\alpha}{2} - i\cos\tfrac{\alpha}{2}\right),\\
c_2 &= -(1-z)\left(M_+ - M_+\kappa_1^{\cos 2}\theta + z\sin^2\theta\left(M_+^* e^{2i\phi}\kappa_2(1+z\kappa_1)\sin^2\tfrac{\alpha}{2} - M_+\kappa_1^{\cos}\alpha\right)\right),\\
c_3 &= -2ze^{i\phi}\sqrt{\kappa_2}(M_z\sqrt{\kappa_1}(1-z) + M_0(1-\sqrt{\kappa_1})(1+z\sqrt{\kappa_1}))\sin\tfrac{\alpha}{2}\sin\theta\left(\cos\theta\sin\tfrac{\alpha}{2} + i\cos\tfrac{\alpha}{2}\right),\\
d_0 &= -z\kappa_2(1-z)(1-\kappa_1)\left(\cos\theta\sin\tfrac{\alpha}{2} - i\cos\tfrac{\alpha}{2}\right)^2,\\
d_1 &= -(1-z)\left(1 + (\kappa_2^2z^2 - \kappa_1^z)\left(\cos^2\tfrac{\alpha}{2} + \cos(2\theta)\sin^2\tfrac{\alpha}{2}\right) - \kappa_1\kappa_2^2z^3\right),\\
d_2 &= -z\kappa_2(1-z)(1-\kappa_1)\left(\cos\theta\sin\tfrac{\alpha}{2} + i\cos\tfrac{\alpha}{2}\right)^2.
\end{aligned} \tag{A.4}$$

The coefficients c_i and d_i are equivalent to those published by Lukzen [26] for the special case of a 90° excitation around the y-axis and arbitrary refocusing around the x-axis. In this case $\phi = 0$, $M_+ = M_0$, and $M_z = 0$. Furthermore, to be consistent with [26] the polar angle θ has to be replaced with $\pi/2 - \theta$. Expression (A.3) now is the z-transform of the magnetization evolution for a single isochromate and needs to be averaged to model the signal in a MESE sequence.

A.2. Averaging over isochromates

For the averaging over isochromates it is best to first consider the approach of decomposing the total magnetization into the configurations [38,31]

$$S(n,U) = \sum_{n=-\infty}^{\infty}\mathbb{F}_k(n)e^{ik\psi} = \sum_{n=-\infty}^{\infty}\mathbb{F}_k(n)u^k \tag{A.5}$$

i.e. the total magnetization $S(n,U)$ is nothing else but a Laurent series with the configurations as coefficients whereas for every n only the zeroth configuration gives rise to an echo. However, the total magnetization is also modelled by $F(z)$ and so $S(n,U)$ can be expressed as the inverse z-transform thereof:

$$S(n,U) = \mathcal{Z}^{-1}\{F(z)\} \tag{A.6}$$

Equating Eqs. (A.5) and (A.6), subsequent z-transform and exploiting linearity of the z-transform

$$\mathcal{Z}\{S(n,U)\} = F(z) = \mathcal{Z}\{\sum_{k=-\infty}^{\infty}\mathbb{F}_k(n)U^k\} = \sum_{k=-\infty}^{\infty}\mathcal{Z}\{\mathbb{F}_k(n)\}U^k \tag{A.7}$$

shows that $F(z)$ is simply the Laurent series of the z-transformed configurations. One now needs to extract the z-transform of the zeroth configuration, i.e. the zeroth coefficient of the Laurent series. As known from complex analysis the closed line integral of a function around a pole gives the coefficient F_{-1} of the corresponding Laurent series: $F_{-1} = 1/(2\pi i)\oint F(U)\mathrm{d}U$ [39]. Thus dividing $F(z,U)$ by U yields the zeroth coefficient of the Laurent series.

$$F_0(z) = \mathcal{Z}\{\mathbb{F}_0(n)\} = \frac{1}{2\pi i}\oint_{|U|=1}\frac{F(z,U)}{U}\mathrm{d}U \tag{A.8}$$

The evaluation of the integral can be elegantly accomplished using the residue theorem [39]

$$F_0(z) = \sum_{m=1}^{M}\mathrm{Res}\left(\frac{F(z,U)}{U}, U_m\right), \tag{A.9}$$

where U_m are the poles of $F(z,U)/U$ that lie inside the unit circle. If U_m is a single pole and $F(z,U)/U$ is of the form $h(z,U)/g(z,U)$ then the residue at U_m can be calculated as

$$\mathrm{Res}\left(\frac{F(z,U)}{U}, U_m\right) = \frac{g(z,U_m)}{h'(z,U_m)}. \tag{A.10}$$

By calculating the roots of the denominator in (A.3) the poles are given as

$$U_0 = 0, \tag{A.11}$$

$$U_{1,2,3,4} = \frac{\mp}{\mp}\frac{\sqrt{-\frac{d_1}{d_2}\frac{\mp}{+}\frac{\sqrt{d_1^2 - 4d_0d_2}}{d_2}}}{\sqrt{2}}. \tag{A.12}$$

Following the method of Lukzen [31] only the poles inside of the unit circle (U_0, U_3, U_4) are used to yield the averaged GF:

$$F_0(z) = \frac{g(z,0)}{U_1U_2U_3U_4} + \frac{g(z,U_3)}{U_3(U_3-U_1)(U_3-U_2)(U_3-U_4)} + \frac{g(z,U_4)}{U_4(U_4-U_1)(U_4-U_2)(U_4-U_3)} \tag{A.13}$$

Carrying out these steps gives

$$F_0(z) = \frac{-2c_2d_0\sqrt{d_1^2-4d_0d_2}+c_0\left(4d_0d_2+d_1\left(-d_1+\sqrt{d_1^2-4d_0d_2}\right)\right)}{2d_0\left(-d_1^2+4d_0d_2\right)} \tag{A.14}$$

and finally

$$F_0(z) = e^{i\phi}\left[\frac{M_x\cos\phi+M_y\sin\phi}{2}\left(1+\sqrt{\frac{X_+(z)}{X_-(z)}}\right)+i\frac{M_y\cos\phi-M_x\sin\phi}{2}\left(1+\sqrt{\frac{X_-(z)}{X_+(z)}}\right)\right] \tag{A.15}$$

$$X_+(z) = (1+z\kappa_2)(1-z(\cos\alpha cos^2\theta+sin^2\theta)(\kappa_1^+ +\kappa_2) + z^2\kappa_1\kappa_2) \tag{A.16}$$

$$X_-(z) = (1-\kappa_2)(1-z(\cos\alpha cos^2\theta+sin^2\theta)(\kappa_1^- -\kappa_2) - z^2\kappa_1\kappa_2) \tag{A.17}$$

If furthermore the initial magnetization is given in spherical coordinates $\overrightarrow{M[0]} = M_0[\cos\phi_e\sin\theta_e, \sin\phi_e\sin\theta_e, \cos\theta_e]^T$ one arrives at the final result given in Eq. (12).

A.3. Derivation of time domain formula

To arrive at a time domain formula $Y_\perp(z) = X_+(z)/X_-(z)$ and $Y_\parallel(z) = X_-(z)/X_+(z)$ have to be inversely z-transformed

$$Y_\perp(z) \overset{z^{-1}}{\bullet\!\!-\!\!\circ} \eta_\perp[n] = g_\perp[n] * g_\perp[n] \quad \text{and} \quad Y_\parallel(z) \overset{z^{-1}}{\bullet\!\!-\!\!\circ} \eta_\parallel[n] = g_\parallel[n] * g_\parallel[n] \tag{A.18}$$

Check poles of $Y_\perp(z)$ and $Y_\parallel(z)$. To do that one has to first have a look at the roots z_{+k} and poles z_{-k} of $Y_\perp(z)$ (the roots of $Y_\perp(z)$ are the poles of $Y_\parallel(z)$). From the definition of the z-transform used in this work, the positioning of all poles outside the unit circle corresponds to a stable and causal system. The poles of $Y_\perp(z)$ all lie on the real axis and are given by the following equations:

$$z_{-1} = \frac{\left((\kappa_2-\kappa_1)\cos\alpha_e - \sqrt{4\kappa_1\kappa_2+(\kappa_1-\kappa_2)^2cos^2\alpha_e}\right)}{2\kappa_1\kappa_2} \tag{A.19}$$

$$z_{-2} = \frac{\left((\kappa_2-\kappa_1)\cos\alpha_e + \sqrt{4\kappa_1\kappa_2+(\kappa_1-\kappa_2)^2cos^2\alpha_e}\right)}{2\kappa_1\kappa_2} \tag{A.20}$$

$$z_{-3} = \frac{1}{\kappa_2} \tag{A.21}$$

where the abbreviation $cos\alpha_e = \cos\alpha sin^2\theta + cos^2\theta$ is used. Given the fact that $0 < \kappa_2 < \kappa_1 < 1$ one can calculate the minimum values for the poles of $Y_\perp(z)$ which are given for all possible values of α by

$$min \quad z_{-1} = -1/\kappa_2 \tag{A.22}$$

$$min \quad z_{-2} = 1/\kappa_1 \tag{A.23}$$

$$min \quad z_{-3} = 1/\kappa_2 \tag{A.24}$$

We can see that all poles lie outside the unit circle and hence conclude the system $Y_\perp(z)$ is both causal and stable for the region of convergence (ROC) being the disk inside the innermost pole [40] (causality being a logical prerequisite for every MR sequence, as no magnetization can be measured before the first RF pulse).

Considering the poles of $Y_\parallel(z)$ the result is similar (whereas the poles can be complex in this case)

$$z_{+1} = \frac{\left((\kappa_2-\kappa_1)\cos\alpha_e - \sqrt{4\kappa_1\kappa_2+(-\kappa_1-\kappa_2)^2cos^2\alpha_e}\right)}{2\kappa_1\kappa_2} \tag{A.25}$$

$$z_{+2} = \frac{\left((\kappa_2-\kappa_1)\cos\alpha_e + \sqrt{4\kappa_1\kappa_2+(-\kappa_1-\kappa_2)^2cos^2\alpha_e}\right)}{2\kappa_1\kappa_2} \tag{A.26}$$

$$z_{+3} = -\frac{1}{\kappa_2} \tag{A.27}$$

with the minimum values also being all outside the unit circle.

$$min \quad z_{+1} = -\frac{1}{\kappa_2} \tag{A.28}$$

$$min \quad z_{+2} = -\sqrt{\frac{1}{\kappa_1\kappa_2}} \tag{A.29}$$

$$min \quad z_{+3} = -\frac{1}{\kappa_2} \tag{A.30}$$

Inverse transform of $Y_\perp(z)$. Upon calculating the inverse transform of $Y_\perp(z)$ we see that the resulting function $\eta_\perp[n]$ is a sum of weighted and shifted versions of another function $\zeta_\perp[n]$.

$$\eta_\perp[n] = \zeta_\perp[n] + (\kappa_2-\kappa_p\cos\alpha_e)\zeta_\perp[n-1] + \kappa_2(\kappa_1-\kappa_p\cos\alpha_e)\zeta_\perp[n-2] + \kappa_1\kappa_2^2\zeta_\perp[n-3] \tag{A.31}$$

$\zeta_\perp[n]$ in turn is a weighted sum of three exponential functions.

$$\kappa_1 = e^{-\tau/T_1} \tag{A.32}$$

$$\kappa_2 = e^{-\tau/T_2} \tag{A.33}$$

$$\kappa_m = \kappa_1 - \kappa_2 \tag{A.34}$$

$$cos\alpha_e = \cos\alpha sin^2\theta + cos^2\theta \tag{A.35}$$

$$S_m = \sqrt{4\kappa_1\kappa_2+\kappa_m^2cos^2\alpha_e} \tag{A.36}$$

$$W_{(m,p)} = (\kappa_m\cos\alpha_e + S_m)/2 \tag{A.37}$$

$$W_{(m,m)} = (\kappa_m\cos\alpha_e - S_m)/2 \tag{A.38}$$

$$w_{m,m} = \kappa_1(-2\kappa_2 + S_m) - \kappa_m \cos\alpha(\kappa_1 - S_m + \kappa_m \cos\alpha_e) \tag{A.39}$$

$$w_{m,p} = \kappa_1(2\kappa_2 + S_m) + \kappa_m \cos\alpha(\kappa_1 + S_m + \kappa_m \cos\alpha_e) \tag{A.40}$$

$$\zeta_\perp[n] = \frac{sec^2(\alpha_e/2)}{4\kappa_m S_m} \cdot \left[-2\kappa_2 S_m \kappa_2^n + w_{m,m} W^n_{(m,m)} + w_{m,p} W^n_{(m,p)}\right] \tag{A.41}$$

As $\eta_\perp[n] = g[n] * g[n]$ is zero for $n < 0$ $g[n]$ can be computed by deconvolution via the following formula:

$$g_\perp[n] = \frac{\eta_\perp[n] - \sum_{k=1}^{n-1} g_\perp[k] g_\perp[n-k]}{2\sqrt{\eta_\perp[0]}} \quad n \geqslant 1 \tag{A.42}$$

Inverse transform of $Y_{||}(z)$**.** The results of $\eta_{||}[n] \overset{z^{-1}}{\bullet\!\!-\!\!\circ} Y_{||}(z)$ are structurally very similar and given by

$$\begin{aligned}\eta_{||}[n] = \zeta_{||}[n] - (\kappa_2 + \kappa_m \cos\alpha)\zeta_{||}[n-1] - \\ \kappa_2(\kappa_1 - \kappa_m \cos\alpha)\zeta_{||}[n-2] + \kappa_1 \kappa_2^2 \zeta_{||}[n-3]\end{aligned} \tag{A.43}$$

The formulas for $\zeta_{||}[n]$ are as follows:

$$\kappa_p = \kappa_1 + \kappa_2 \tag{A.44}$$

$$S_p = \sqrt{-4\kappa_1\kappa_2 + \kappa_p^2 cos^2\alpha_e} \tag{A.45}$$

$$W_{(p,p)} = (\kappa_p \cos\alpha_e + S_p)/2 \tag{A.46}$$

$$W_{(p,m)} = (\kappa_p \cos\alpha_e - S_p)/2 \tag{A.47}$$

$$w_{p,p} = \kappa_1(-2f\kappa_2 + S_p) + \kappa_p \cos\alpha_e(\kappa_1 + S_p + \kappa_p \cos\alpha_e) \tag{A.48}$$

$$w_{p,m} = \kappa_1(2\kappa_2 + S_p) - \kappa_p \cos\alpha_e(\kappa_1 - S_p + \kappa_p \cos\alpha_e) \tag{A.49}$$

$$\zeta_{||}[n] = \frac{\sec^2(\alpha_e/2)}{4\kappa_p S_p} \cdot [2\kappa_2 S_p(-\kappa_2)^n + w_{p,p} W^n_{(p,p)} + w_{p,m} W^n_{(p,m)}] \tag{A.50}$$

Finally, the deconvolution formula for $g_{||}[n]$ is essentially the same as for $g_\perp[n]$

$$g_{||}[n] = \frac{\eta_{||}[n] - \sum_{k=1}^{n-1} g_{||}[k] g_{||}[n-k]}{2\sqrt{\eta_{||}[0]}} \quad n \geqslant 1 \tag{A.51}$$

Special case for $\alpha_e = \pi$**.** In case the refocusing angle $\alpha_e = \pi$ the $sec(\alpha_e/2)$ becomes infinity. Computing the limit for both $\eta_\perp$ and $\eta_{||}$ yields

$$\lim_{\alpha_e \to \pi} \eta_\perp[n] = 4n\kappa_2{}^n \tag{A.52}$$

$$\lim_{\alpha_e \to \pi} \eta_{||}[n] = 4n(-\kappa_2)^n \tag{A.53}$$

which are the convolution of an exponential decay and an alternating sign exponential decay function, respectively.

$$g_\perp[n] = 2\kappa_2{}^n \tag{A.54}$$

$$g_{||}[n] = 2(-\kappa_2)^n \tag{A.55}$$

This is exactly what would be expected for a 180° pulse for a CPMG and CP sequence. Putting it all together, the evolution of the magnetization for this limiting case is given by

$$M_+[n] = M_0 e^{i\phi} \sin\theta_e \left[cos(\phi_e - \phi) - \kappa_2{}^n + i\sin(\phi_e - \phi)(-\kappa_2)^n\right] \quad n \geqslant 0. \tag{A.56}$$

References

[1] T.J. Mosher, B.J. Dardzinski, Cartilage MRI T relaxation time mapping: overview and applications, Seminars Musculosk. Radiol. 8 (4) (2004) 355–368. http://www.ncbi.nlm.nih.gov/pubmed/15643574, https://doi.org/10.1055/s-2004-861764.

[2] T.G. St, P.R. Pierre, W. Clark, A.J. Chua-anusorn, G.P. Fleming, J.K. Jeffrey, P. Olynyk, E. Pootrakul, R Lindeman Robins, Noninvasive measurement and imaging of liver iron concentrations using proton magnetic resonance, Blood 105 (2) (2005) 855–861. http://bloodjournal.hematologylibrary.org/content/105/2/855, https://doi.org/10.1182/blood-2004-01-0177.

[3] N.R. Ghugre, V. Ramanan, M. Pop, Y. Yang, J. Barry, B. Qiang, K.A. Connelly, A.J. Dick, G.A. Wright, Myocardial BOLD imaging at 3 T using quantitative T: application in a myocardial infarct model, Magnet. Reson. Med. 66 (6) (2011) 1739–1747. http://onlinelibrary.wiley.com/doi/10.1002/mrm.22972/abstract, https://doi.org/10.1002/mrm.22972.

[4] M. Neema, J. Stankiewicz, A. Arora, V.S. Dandamudi, C.E. Batt, Z.D. Guss, A. Al-Sabbagh, R. Bakshi, T- and T-based MRI measures of diffuse gray matter and white matter damage in patients with multiple sclerosis, J. Neuroimaging 17 (2007) 16–21. http://onlinelibrary.wiley.com/doi/10.1111/j.1552-6569.2007.00131.x/full, https://doi.org/10.1111/j.1552-6569.2007.00131.x.

[5] S. Ropele, W. de Graaf, M. Khalil, M.P. Wattjes, C. Langkammer, M.A. Rocca, A. Rovira, J. Palace, F. Barkhof, M. Filippi, F. Fazekas, MRI assessment of iron deposition in multiple sclerosis, J. Magnet. Reson. Imaging 34 (1) (2011) 13–21. http://onlinelibrary.wiley.com/doi/10.1002/jmri.22590/pdf, https://doi.org/10.1002/jmri.22590.

[6] S. Majumdar, S.C. Orphanoudakis, A. Gmitro, M. O'Donnell, J.C. Gore, Errors in the measurements of T using multiple-echo MRI techniques. I. Effects of radiofrequency pulse imperfections, Magnet. Reson. Med. 3 (3) (1986) 397–417.

[7] S. Majumdar, J.C. Gore, Effects of selective pulses on the measurement of T and apparent diffusion in multiecho MRI, Magnet. Reson. Med. 4 (2) (1987) 120–128.

[8] A. Petrovic, E. Scheurer, R. Stollberger, Closed-form solution for T mapping with nonideal refocusing of slice selective CPMG sequences, Magnet. Reson. Med. 73 (2) (2015) 818–827. http://onlinelibrary.wiley.com/doi/10.1002/mrm.25170/abstract, https://doi.org/10.1002/mrm.25170.

[9] P.A. Boulby, F.J. Rugg-Gunn, T: The transverse relaxation time, in: P. Tofts (Ed.), Quantitative MRI of the Brain, John Wiley & Sons, Ltd, 2003. Htpps://doi.org/10.1002/0470869526. URL https://onlinelibrary.wiley.com/doi/book/10.1002/0470869526.

[10] J. Zhu, A. Bornstedt, N. Merkle, N. Liu, W. Rottbauer, G. Ma, V. Rasche, T-prepared segmented 3 D-gradient-echo for fast T-weighted high-resolution three-dimensional imaging of the carotid artery wall at 3 T: a feasibility study, BioMed. Eng. OnLine 15 (2) (2016) 165, https://doi.org/10.1186/s12938-016-0276-9.

[11] P.A. Gowland, A. Freeman, B. Issa, P. Boulby, K.R. Duncan, R.J. Moore, P.N. Baker, R.W. Bowtell, I.R. Johnson, B.S. Worthington, In vivo relaxation time measurements in the human placenta using echo planar imaging at 0.5 T, Magnet. Reson. Imaging 16 (3) (1998) 241–247. http://www.sciencedirect.com/science/article/pii/S0730725X97003081, https://doi.org/10.1016/S0730-725X(97)00308-1.

[12] S.C. Deoni, Transverse relaxation time (T) mapping in the brain with off-resonance correction using phase-cycled steady-state free precession imaging, J. Magnet. Reson. Imaging 30 (2) (2009) 411–417. http://onlinelibrary.wiley.com/doi/10.1002/jmri.21849/abstract, https://doi.org/10.1002/jmri.21849.

[13] H.Y. Carr, E.M. Purcell, Effects of diffusion on free precession in nuclear magnetic resonance experiments, Phys. Rev. 94 (3) (1954) 630. http://link.aps.org/doi/10.1103/PhysRev.94.630, https://doi.org/10.1103/PhysRev.94.630.

[14] S. Meiboom, D. Gill, Modified spin-echo method for measuring nuclear relaxation times, Rev. Sci. Instrum. 29 (1958) 688–691.

[15] S. Majumdar, A. Gmitro, S.C. Orphanoudakis, D. Reddy, J.C. Gore, An estimation and correction scheme for system imperfections in multiple-echo magnetic resonance imaging, Magn. Reson. Med. 4 (3) (1987) 203–220.

[16] A.P. Crawley, R.M. Henkelman, Errors in T_2 estimation using multislice multiple-echo imaging, Magn. Reson. Med. 4 (1) (1987) 34–47.

[17] S.T. Wong, M.S. Roos, Effects of slice selection and diffusion on T_2 measurement, Magn. Reson. Med. 5 (4) (1987) 358–365.

[18] M.H. Levitt, R. Freeman, Compensation for pulse imperfections in NMR spin-echo experiments, J. Magn. Reson. 43 (1981) 65–80.

[19] A.A. Maudsley, Modified Carr-Purcell-Meiboom-Gill sequence for NMR Fourier imaging applications, J. Magn. Reson. 69 (1986) 488–491.

[20] Y. Zur, S. Stokar, A phase-cycling technique for canceling spurious echoes in NMR imaging, J. Magn. Reson. 71 (1987) 212–228.

[21] C.S. Poon, R.M. Henkelman, Practical T quantitation for clinical applications, J. Magn. Reson. Imaging 2 (5) (1992) 541–553.

[22] J.G. Sled, G.B. Pike, Correction for B and B variations in quantitative T_2 measurements using MRI, Magn. Reson. Med. 43 (2000) 589–593.

[23] G.S. Pell, R.S. Briellmann, A.B. Waites, D.F. Abbott, D.P. Lewis, G.D. Jackson, Optimized clinical T relaxometry with a standard CPMG sequence, J. Magn. Reson. Imaging 23 (2) (2006) 248–252. http://onlinelibrary.wiley.com/doi/10.1002/jmri.20490/abstract, https://doi.org/10.1002/jmri.20490.

[24] N. Ben-Eliezer, D.K. Sodickson, K.T. Block, Rapid and accurate T_2 mapping from multi-spin-echo data using Bloch-simulation-based reconstruction, Magn.

Reson. Med. 73 (2) (2015) 809–817. http://onlinelibrary.wiley.com/doi/10.1002/mrm.25156/abstract, https://doi.org/10.1002/mrm.25156.
[25] R.M. Lebel, A.H. Wilman, Transverse relaxometry with stimulated echo compensation, Magn. Reson. Med. 64 (4) (2010) 1005–1014. http://onlinelibrary.wiley.com/doi/10.1002/mrm.22487/abstract, https://doi.org/10.1002/mrm.22487.
[26] N.N. Lukzen, M.V. Petrova, I.V. Koptyug, A.A. Savelov, R.Z. Sagdeev, The generating functions formalism for the analysis of spin response to the periodic trains of RF pulses. Echo sequences with arbitrary refocusing angles and resonance offsets, J. Magn. Reson. 196 (2) (2009) 164–169, https://doi.org/10.1016/j.jmr.2008.11.008.
[27] B. Buttkus, Spectral Analysis and Filter Theory in Applied Geophysics, Springer Science & Business Media, 2012 (Chapter 6).
[28] J. Pauly, P. Le Roux, D. Nishimura, A. Macovski, Parameter relations for the Shinnar-Le Roux selective excitation pulse design algorithm, IEEE Trans. Med. Imaging 10 (1991) 53–65.
[29] K.P. Whittall, A.L. Mackay, D.A. Graeb, R.A. Nugent, D.K.B. Li, D.W. Paty, In vivo measurement of T_2 distributions and water contents in normal human brain, Magn. Reson. Med. 37 (1) (1997) 34–43. https://onlinelibrary.wiley.com/doi/abs/10.1002/mrm.1910370107, https://doi.org/10.1002/mrm.1910370107.
[30] A. Lesch, M. Schloegl, M. Holler, K. Bredies, R. Stollberger, Ultrafast 3d Bloch-Siegert B-mapping using variational modeling, Magnet. Reson. Med. 81 (2) (2019) 881–892. https://onlinelibrary.wiley.com/doi/abs/10.1002/mrm.27434, https://doi.org/10.1002/mrm.27434.
[31] N.N. Lukzen, A.A. Savelov, Analytical derivation of multiple spin echo amplitudes with arbitrary refocusing angle, J. Magn. Reson. 185 (1) (2007) 71–76, https://doi.org/10.1016/j.jmr.2006.11.010.
[32] G.J. Stanisz, E.E. Odrobina, J. Pun, M. Escaravage, S.J. Graham, M.J. Bronskill, R. M. Henkelman, T_1, T_2 relaxation and magnetization transfer in tissue at 3 T, Magn. Reson. Med. 54 (3) (2005) 507–512. https://onlinelibrary.wiley.com/doi/abs/10.1002/mrm.20605, https://doi.org/10.1002/mrm.20605.
[33] I. Blystad, J.B.M. Warntjes, R. Smedby, P. Lundberg, E.-M. Larsson, A. Tisell, Quantitative MRI for analysis of peritumoral edema in malignant gliomas, PLOS ONE 12 (5) (2017). https://journals.plos.org/plosone/article?id=10.1371/journal.pone.0177135, https://doi.org/10.1371/journal.pone.0177135.
[34] J.M. Spijkerman, E.T. Petersen, J. Hendrikse, P. Luijten, J.J.M. Zwanenburg, T2 mapping of cerebrospinal fluid: 3 T versus 7 T, Magma (New York, N.y.) 31 (3) (2018) 415–424. https://www.ncbi.nlm.nih.gov/pmc/articles/PMC5973950/, https://doi.org/10.1007/s10334-017-0659-3.
[35] R. Stollberger, P. Wach, Imaging of the active B field in vivo, Magn. Reson. Med. 35 (2) (1996) 246–251. http://onlinelibrary.wiley.com/doi/10.1002/mrm.1910350217/abstract, https://doi.org/10.1002/mrm.1910350217.
[36] F.S. Acton, Numerical Methods that Work, The Mathematical Association of America, Washington, D.C., 1997.
[37] T.J. Sumpf, A. Petrovic, M. Uecker, F. Knoll, J. Frahm, Fast T_2 Mapping with improved accuracy using undersampled spin-echo MRI and model-based reconstructions with a generating function, IEEE Trans. Med. Imaging 33 (12) (2014) 2213–2222, https://doi.org/10.1109/TMI.2014.2333370.
[38] M. Weigel, Extended phase graphs: dephasing, RF pulses, and echoes - pure and simple, J. Magn. Reson. Imaging 41 (2) (2015) 266–295. http://onlinelibrary.wiley.com/doi/10.1002/jmri.24619/abstract, https://doi.org/10.1002/jmri.24619.
[39] O. Follinger, Laplace-, Fourier- und z-Transformation, seventh ed., Huthig Verlag, Heidelberg, 2000 (Chapter 7).
[40] A.V. Oppenheim, R.W. Schafer, Discrete-Time Signal Processing, third ed., Prentice Hall, Upper Saddle River, NJ, 2007.